Check for updates

ADVANCED MATERIALS
www.advmat.de

Out-of-Plane Electronics on Flexible Substrates Using Inorganic Nanowires Grown on High-Aspect-Ratio Printed Gold Micropillars

*Sihang Ma, Abhishek Singh Dahiya, and Ravinder Dahiya**

Out-of-plane or 3D electronics on flexible substrates are an interesting direction that can enable novel solutions such as efficient bioelectricity generation and artificial retina. However, the development of devices with such architectures is limited by the lack of suitable fabrication techniques. Additive manufacturing (AM) can but often fail to provide high-resolution, sub-micrometer 3D architectures. Herein, the optimization of a drop-on-demand (DoD), high-resolution electrohydrodynamic (EHD)-based jet printing method for generating 3D gold (Au) micropillars is reported. Libraries of Au micropillar electrode arrays (MEAs) reaching a maximum height of 196 µm and a maximum aspect ratio of 52 are printed. Further, by combining AM with the hydrothermal growth method, a seedless synthesis of zinc oxide (ZnO) nanowires (NWs) on the printed Au MEAs is demonstrated. The developed hybrid approach leads to hierarchical light-sensitive NW-connected networks exhibiting favorable ultraviolet (UV) sensing as demonstrated via fabricating flexible photodetectors (PDs). The 3D PDs exhibit an excellent omnidirectional light-absorption ability and thus, maintain high photocurrents over wide light incidence angles (±90°). Lastly, the PDs are tested under both concave and convex bending at 40 mm, showing excellent mechanical flexibility.

1. Introduction

Flexible and printed electronics have attracted considerable attention in the past decade due to interesting applications such as rollable displays, wearable systems for healthcare, intelligent identification tags, electronic skin for robotics, prosthetics, and implantable systems.[1] Thus far, the research in the field has mainly focused on the integration of various building blocks such as sensors, transistors, interconnects, etc., on the same substrate and in the same plane.[2] Transforming the current planar integration of electronic devices into 3D or out-of-plane configuration could create attractive new opportunities for the advancement of this exciting field into diverse ranges of applications such as drug delivery, tissue engineering, surface engineering, optoelectronics, energy conversion, and storage, etc.[3] For instance, hemispherical silicon nanorod photodiode arrays have been used to extract the angular information of light in a 3D space to enable imaging systems with a wide field of view, miniaturized design, and deep depth of field.[4] The additional attributes of out-of-plane configurations endow flexible electronic system with an enhanced sensing surface area, large stretchability, and high-device integration density.[5] Owing to such features, the out-of-plane structures such as micro/nanopillars, nanowires (NWs), scaffolds, etc., have attracted attention.[6,7]

Various fabrication methods have been explored to construct out-of-plane architectures on planar substrates. These include conventional subtractive microfabrication, lithography, high-vacuum deposition processes, and chemical etching.[8] Often these fabrication strategies are complex and not suitable for flexible substrates. Further, they are time consuming, resource-insufficient, leading to considerable chemical wastage and high cost due to the involvement of vacuum systems.[9,10] These conventional approaches could be replaced by the additive manufacturing (AM), which involves the use of printing technologies for a direct deposition of out-of-plane structures. However, most of the existing AM techniques offer a poor resolution and it is challenging to obtain structures (e.g., micro/nanopillars) with diameters of <50 µm.[11] In this regard, the high-resolution jet-based printing technique has shown good potential. For instance, aerosol jet printing has been used to produce micropillar electrode arrays (MEAs) for photosynthetic applications.[12] These out-of-plane MEAs have helped to achieve the state-of-the-art photocurrent densities of 245 µA cm^{-2} and external quantum efficiencies of up

S. Ma, A. S. Dahiya
James Watt School of Engineering
University of Glasgow
Glasgow G12 8QQ, UK
R. Dahiya
Bendable Electronics and Sustainable Technologies (BEST) Group
Electrical and Computer Engineering Department
Northeastern University
Boston, MA 02115, USA
E-mail: r.dahiya@northeastern.edu

The ORCID identification number(s) for the author(s) of this article can be found under https://doi.org/10.1002/adma.202210711

© 2023 The Authors. Advanced Materials published by Wiley-VCH GmbH. This is an open access article under the terms of the Creative Commons Attribution License, which permits use, distribution and reproduction in any medium, provided the original work is properly cited.

DOI: 10.1002/adma.202210711

Table 1. Comparison of EHD-based jet-printed nano- to microscale pillars.

Diameter	Height	Aspect Ratio	Ink	Substrate	Application	Reference
12 μm	100μm	8	Wax	N/A	–	[18]
≈200 μm	0.7–1.8 mm	3.5–9	Molten metal (32.5% bismuth, 51% indium, 16.5% tin)	PDMS, Glass	Interconnects	[19]
1.4 μm	66 μm	50	Ag	Plastic, flexible	Interconnects	[6]
20 μm	120 μm	6	Ag	N/A	–	[20]
–	–	35	Ag	Si wafer and glass coverslip	Touch sensor and air flow-rate sensor	[15]
170 nm – Cu	65 μm – Cu	400 – Cu	Ag, Cu, Ag–Cu	Glass slides and Si wafers	–	[21]
3 μm	75 μm	25	Au	Rigid glass slide & MEA	Cellular activity monitoring	[13]
50 nm	850 nm	17	Au	Glass	Plasmonics	[22]
3.74 μm	196 μm	52.47	Au	Flexible polyimide	Out-of-plane ZnO-nanostructure-based photodetectors	This work

to 29%. The aerosol jet printing with a resolution of 10–15 μm can provide out-of-plane structures with a larger height (>500 μm), but fails to deliver the same with a high aspect ratio. High-aspect-ratio 3D structures are needed to achieve the high-density device integration for large sensing areas. In this regard, the drop-on-demand (DoD), electrohydrodynamic (EHD)-based jet printing has garnered significant attention. The method involves the dropwise dispensing of a nanoparticle laden ink from a scanning nozzle.[13–15] Such printing systems are usually computer-interfaced, and they enable a mask-less fabrication, allowing a greater flexibility for building out-of-plane self-supporting structures such as micro- and nanoscale pillars. High resolution EHD printing systems have therefore been explored for achieving 3D structures; however, the choice of printing materials is mainly limited to forming metallic structures with a small aspect ratio. **Table 1** shows EHD-printed out-of-plane structures and a comparison regarding the aspect ratio, length, type of inks, substrates, and applications developed.

Herein, we report a novel fabrication route to obtain out-of-plane hierarchical functional (light sensitive) nanoarchitectures comprising DoD EHD-printed high-aspect-ratio conductive micropillars followed by out-of-plane seedless growth of zinc oxide (ZnO) NWs on micropillars using a low-temperature hydrothermal (HT) growth method.[10,16] The EHD printing method has been optimized, in terms of applied voltage, frequency, stage speed, and nozzle-to-substrate distance, to obtain directly printed high-aspect-ratio (ultralong with short diameters) metallic micropillars. The optimized EHD process has allowed us to print libraries of gold (Au) MEAs with different heights, diameters, and pitches. Maximum micropillars, a height of ≈196 μm with an aspect ratio of ≈52, have been achieved. Following this, a seedless HT growth of ZnO NWs has been carried out on printed Au MEAs. To the best of our knowledge, this is the first study where a seedless HT growth of ZnO NWs is carried out on printed 3D Au micropillars. As a proof of concept, these light-sensitive hierarchical structures have been used to obtain out-of-plane 3D flexible ultraviolet (UV) photodetectors (PDs). The 3D PDs, formed with the optimized micropillar spacing, have shown one of the best photoresponsive performances, including detectivity (2.62×10^{17} Jones), responsivity (3.16×10^5 A W^{-1}) and external quantum efficiency (1.06×10^8%) at low bias voltage (0.1 V) and light intensity (1 μW cm^{-2}). Further, compared to 2D layouts, the fabricated 3D PDs have shown better sensitivity and an excellent omnidirectional light-absorption ability. The developed PDs maintain high photocurrents over wide light incident angles (±90°), which is needed to enable broadband omnidirectional UV light detection. The 3D PDs have also been tested under both concave and convex bending conditions and demonstrated excellent mechanical flexibility as well as negligible changes in device performance under mechanical loadings. The presented hierarchical 3D-connected NW network could also enhance the energy harvesting efficiency of solar cells and the artificial photosynthesis process by light scattering enhancement and trapping.[12,17]

2. Results and Discussion

2.1. Printed Micropillar Arrays

The EHD-based jet printing is an AM technique that can print metal and/or functional nanoparticle inks with high design flexibility and resolution via a contactless direct write approach. In this work, EHD-based super inkjet (SIJ) printer is employed, as shown schematically in **Figure 1**a. During printing, the nozzle is positioned few micrometers (20–40 μm) above a three-axis motorized stage on which the substrate is placed. As per the EHD mechanism, the computer-interfaced system generates force to eject droplets through an oscillating electric field between the nozzle and the printing stage, controlled by the voltage applied. It is to note that, in comparison with the conventional EHD printing, SIJ does not form a Taylor cone that limits the process controllability.[23] As a result, SIJ has precise control over the volume of the ink droplet. The minimum volume of ink droplets is 0.1 fL, that is, 1/1000 times smaller than that of a conventional inkjet printer (volume = 2 pL or diameter = 16 μm).[24] Further, the volume of the droplet and/or the printing resolution can be changed or optimized by varying the applied frequency, the stage speed, and the distance between the nozzle tip and the substrate. For example, the printing frequency becomes critical for the construction of micropillars when the ejected droplets are required to be vertically stacked. Frequency is important because it controls the time interval between the consecutive droplets. For the pillar formation, each incoming droplet needs to be viscous enough to

© 2023 The Authors. Advanced Materials published by Wiley-VCH GmbH

15214095, 2023, 26, Downloaded from https://onlinelibrary.wiley.com/doi/10.1002/adma.202210711 by Test, Wiley Online Library on [07/07/2023]. See the Terms and Conditions (https://onlinelibrary.wiley.com/terms-and-conditions) on Wiley Online Library for rules of use; OA articles are governed by the applicable Creative Commons License

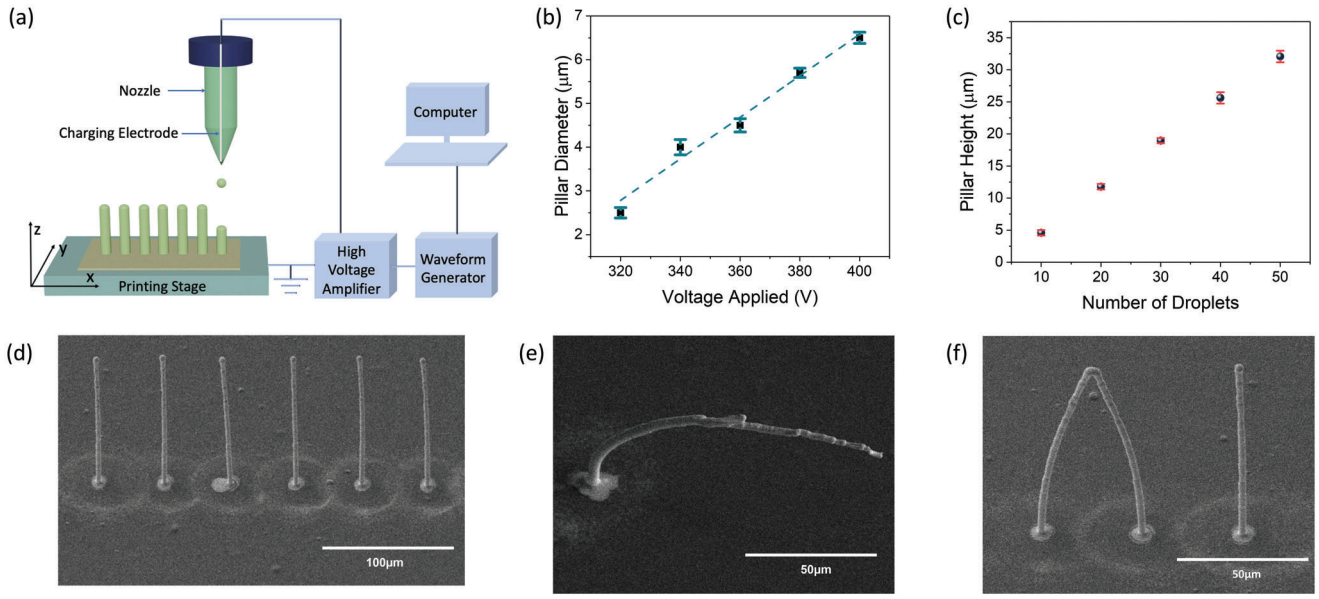

Figure 1. a) The EHD micropillar printing schematic. b) Change of pillar diameter as a function of the applied voltage. c) Change of pillar height as a function of the number of droplets. d–f) SEM images of linear array of high-aspect-ratio micropillars (d), a tilted pillar (e); and an arch-shaped pillar (f).

avoid spreading (i.e., most of the solvent must evaporate before arriving on the pillar/substrate). The optimized frequency provides enough time for the previous droplet to dry and hence to maintain its shape. Therefore, the optimization of each printing parameter is critical for a sequence of droplet deposition and liquid vaporization to achieve a high aspect ratio and uniform out-of-plane micropillars.

In this work, printed micropillars were obtained using superfine nozzles (1–3 μm diameter opening size) with gold nanoparticle (Au NP) ink under ambient and controlled conditions (room temperature between 20 and 23 °C, relative humidity (RH): ≈40%). The optimization process is as follows: one of the most critical printing parameters is the applied voltage, which directly determines the electric field strength needed to eject the droplet from the nozzle. Primarily, the applied voltage needs to be large enough to eject droplets. A higher electric field leads to a higher jetting speed and higher volume of the jetted ink per droplet, therefore leading to larger printed features. Further, higher jetting speed results in a shorter flight time of the ejected droplets, providing less time to evaporate the ink solvent and thus, poor control over the micropillar's diameter. Besides, higher voltages could lead to ink spreading at the bottom of the pillar, potentially short-circuiting the adjacent pillars. Figure 1b and Figure S1a–c (Supporting Information) show the influence of the change in applied voltage on the diameter of micropillars. The data show a directly proportional relationship between the applied voltage and the diameter of micropillars. Other important printing parameters are the stage speed, frequency of applied voltage, and the nozzle to substrate distance. To construct MEAs, it is important to control the stage speed as it is dependent on the desired pillar spacing. A lower printing speed is more suited to achieve MEAs with smaller pitches as it provides a longer flight time and hence allows the solvent to dry before the subsequent droplet reaches on top of the previous one. Likewise, the frequency of applied voltage is directly related to the liquid vaporization rate. The optimized printing frequency and speed used in this work to construct MEAs were 20 Hz and 1 mm s^{-1}, respectively. It is to note that the printing acceleration was fixed to 10 mm s^{-2}. The nozzle-tosubstrate distance was optimized to be ≈20 μm for a stable printing.

Next, we recorded the change in micropillar height with respect to the number of droplets. Figure 1c and Figure S1d (Supporting Information) show the plots of measured micropillar heights with an increasing number of droplets applied (from 10 to 50). Figure S1e (Supporting Information) depicts the scanning electron microscopy (SEM) image of five rows of printed micropillars obtained with different numbers of droplets (10–50 droplets from the bottom to the top in the image). It was observed that the micropillar started to appear after five droplets (Figure S1f, Supporting Information, a pillar formed by 10 droplets). After the pillar "base" is built, the average pillar growth rate is ≈0.5 μm per droplet. To avoid nozzle clogging and to ensure uniform growth of micropillars, the nozzle distance from the substrate was increased during printing in such a way that there was some distance between the micropillar tip and the nozzle. For this, the nozzle was moved up along the *z*-axis by 10 μm for every 20 droplets (corresponding to ≈0.5 μm per droplet). After printing, the micropillars were annealed at 250 °C for 2 h to cure the ink. Using the above-mentioned optimized parameters, in the case of MEA printing, taking the stage movement into account, a micropillar printed through 50 droplets (≈22.5 μm) can be generated in ≈5–6 s. Figure 1d shows the SEM image of MEAs resulting from the optimized printing parameters with the state-of-the-art aspect ratio (height = 196 μm, diameter = 3.74 μm, aspect ratio = 52.47). (Note: the SEM images are taken with the sample held at 45°; hence, the actual pillar height = (pillar height in SEM images)/sin(45°)). Figure 1e shows a tilted micropillar obtained by moving the printing stage along the *x*-axis. This can be achieved owing to the autofocusing effect. During printing, the top of the pillar can serve as a charged electrode, which

© 2023 The Authors. Advanced Materials published by Wiley-VCH GmbH

15214095, 2023, 26, Downloaded from https://onlinelibrary.wiley.com/doi/10.1002/adma.202210711 by Test, Wiley Online Library on [07/07/2023]. See the Terms and Conditions (https://onlinelibrary.wiley.com/terms-and-conditions) on Wiley Online Library for rules of use; OA articles are governed by the applicable Creative Commons License

can generate electric field gradients and attract the approaching droplets toward the already printed structure instead of the substrate. An array of tilted pillar formed with different number of droplets is shown in Figure S1g (Supporting Information). Subsequently, free-standing arch-shaped structures were realized by controlling the direction of substrate movement (Figure 1f; Figure S1h, Supporting Information). The demonstrated capability to achieve different shapes of high-resolution, freestanding out-of-plane structures reflects the versatility of the presented printing approach, which can also assist in the development of new solutions for 3D interconnects, vias, extracting light's angular information in 3D space and so on.

2.2. Out-of-Plane MEA-ZnO NW Network-Based Photodetectors

The printed MEAs were used to realize 3D hierarchical light sensitive NW-network for omnidirectional light harvesting. For this, a seedless hydrothermal (HT) growth approach was used to grow out-of-plane ZnO NWs on printed MEAs. To validate the omnidirectional light detection, the UV photodetectors (PDs) were realized on flexible polyimide (PI) substrates using the 3D hierarchical NW-network. First, the pillar pitch was optimized to have the best UV sensing performance. For this, Au contact electrodes with 100 µm channel length were first printed. Then, one row of micropillars was printed in between the printed contact electrodes. Please note that the device contact electrodes are connected to the ZnO NWs through micropillars on the electrodes. Pillar arrays with three different pitches (10, 15, and 20 µm) were fabricated to explore the effect of 3D micropillar pitches on PD performance. Next, ZnO NWs were hydrothermally grown (see Experimental Section for details on NW synthesis).

The electrical characterization of as-fabricated PDs was performed using a UV light-emitting diode (365 nm) under ambient conditions. To have the statistical data, five devices for each pillar pitch were characterized under similar conditions: 1 µW cm^{-2} light illumination and 1 V bias voltage. The obtained experimental results are shown in Figure S2 (Supporting Information). **Figure 2**a–c depicts the time-domain photoresponse of fabricated PDs with different pillar pitches at 1 V bias under varying illumination intensities from 0.5 to 2.5 µW cm^{-2} with a step of 0.5 µW cm^{-2}. In all the cases, the photocurrent increases with the increment of incident UV light intensities, because of higher electron–hole pair generation. Further, key parameters including responsivity (R), specific detectivity (D^*), external quantum efficiency (EQE), and I_{light}/I_{dark} ratio were extracted from the photoresponse curves at different light intensities (Figure S3, Supporting Information). Responsivity (R) is calculated to study the photocurrent response to the incident light using this expression:

$$R = \frac{\left(I_{\text{Light}} - I_{\text{Dark}}\right)}{\left(P_{\text{in}} \times S\right)} \tag{1}$$

where I_{Light} stands for the current under UV light, I_{Dark} is the current under dark condition, P_{in} is the incident light power per unit area (from 0.5 to 2.5 µW cm^{-2}), and S is the effective sensing area of the device (channel length = 100 µm, channel width = 13 µm including the pillar diameter and NW length, $S = 1.3 \times 10^{-5}$cm^2). The specific detectivity (D^*) is obtained to study the device capability of detecting the smallest signals using this equation:

$$D^* = \frac{R}{\sqrt{2eJ_{\text{Dark}}}} \tag{2}$$

where e is the elementary charge and J_{Dark} is the current density during the dark condition. Next, the EQE is derived to assess the optical properties using:[25]

$$\text{EQE} = \frac{R \times hc}{e\lambda} \times 100 \tag{3}$$

where c represents the velocity of light and λ is the wavelength of incident light. Finally, the photocurrent on/off ratio is extracted for PDs with 10, 15, and 20 µm micropillar pitches. Extracted parameters are shown in Figure 2d,e to compare three different configurations. The 15 µm spaced micropillar-based PDs show the best performance among these samples, exhibiting $R = 6.31 \times 10^5$ A W^{-1} (Figure 2d), $D^* = 1.27 \times 10^{16}$ Jones (Figure 2d), EQE $= 2.11 \times 10^8$% (Figure 2e), and $I_{\text{photo}}/I_{\text{dark}} = 41$ (Figure 2e) at the light intensity of 1 µW cm^{-2} and 1 V bias. It is to note that the sensing channel length and applied bias voltage were fixed for all the samples. The experimentally obtained results can be explained using the following hypothesis. The sensing mechanism is described using an energy band diagram schematic shown in Figure 2f. Under no UV light illumination, oxygen molecules exist on the NW surface, forming an electron depletion layer on the NW surface. The near-surface depletion layer results in an upward band bending and therefore forms energy barriers at the metal–semiconductor (MS) interfaces. In all device cases (i.e., PDs with 10, 15, and 20 µm micropillar pitches), devices structured by the row of pillars in series and grown NWs on them form countless NW–NW junctions between the sensing channels. Each NW–NW junction can be represented with a potential energy barrier encountered by the charge carriers under a fixed voltage bias. Under UV illumination, the large number of electron–hole pairs is formed, leaving holes in the valence band and excited electrons to the conduction band. Furthermore, the generated hole reacts with the adsorbed oxygen ions on the surface and results in the desorption of oxygen molecules and the release of free electrons. Both events lead to a decrease in the depletion width ($W_{\text{depletion}}$ shown in Figure 2f) at the MS interface and NW–NW junctions. Likewise, the barrier becomes largely transparent to the incoming free charge carriers and leads to an exponential increase in the device current. With the fixed channel length for all cases (100 µm channel length for PDs with 10, 15, and 20 µm micropillar pitches), there will be a higher number of pillars in the sensing channel for devices with 10 µm spaced micropillars. The higher number of pillars in these devices will provide higher nucleation sites for growth of NWs, leading to greater number of NW–NW junctions. This also results in extra energy barriers and reduced dark current. Conversely, devices with 20 µm pillar pitches possess less NW–NW junctions, causing electrons to travel in less barriers and therefore leading to a higher dark current and longer recovery time. In addition, using the abovementioned HT ZnO NWs growth method, the NW length is ≈5 µm. Considering the micropillar diameter (≈3 µm), devices with 15 µm pillar spacing allow a more suitable space for

© 2023 The Authors. Advanced Materials published by Wiley-VCH GmbH

15214095, 2023, 26, Downloaded from https://onlinelibrary.wiley.com/doi/10.1002/adma.202210711 by Test, Wiley Online Library on [07/07/2023]. See the Terms and Conditions (https://onlinelibrary.wiley.com/terms-and-conditions) on Wiley Online Library for rules of use; OA articles are governed by the applicable Creative Commons License

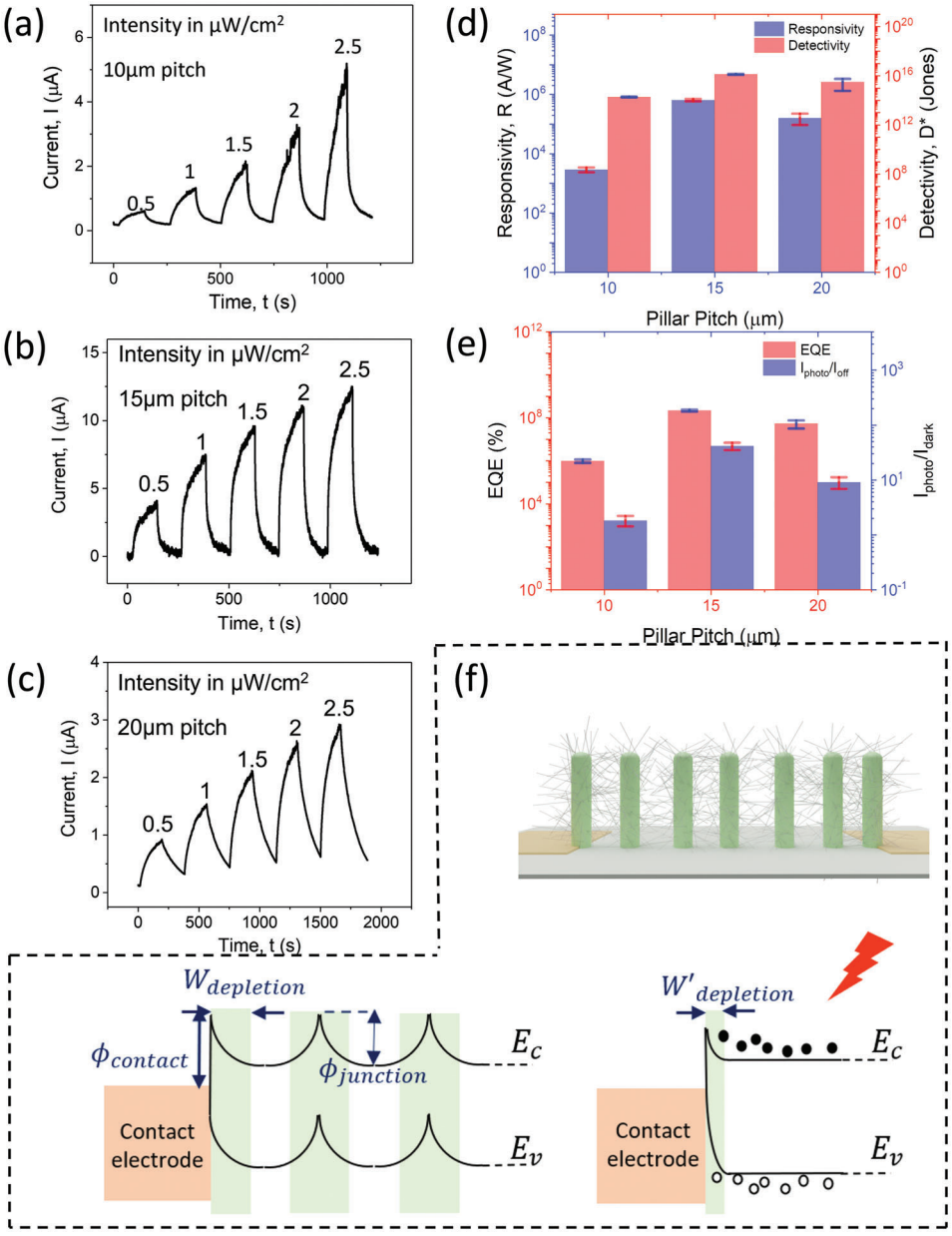

Figure 2. a–c) Time-domain photoresponse of fabricated out of plane PDs at 1 V bias under increased illumination intensities from 0.5 to 2.5 μW cm^{-2} with a step of 0.5 μW cm^{-2} and different pillar pitches: a) 10 μm pillar pitch; b) 15 μm pillar pitch; c) 20 μm pillar pitch; d,e) Extracted parameters: d) responsivity and detectivity; e) extracted EQE and I_{photo}/I_{dark}. f) Schematic of as-fabricated PD and energy band diagram under dark and UV conditions showing the sensing mechanism.

NW growth, resulting in the most desirable scenario to achieve the optimal high sensing performance. The *I–V* characteristics (both in linear and log scales) for the 15 μm pillar pitch device, under dark and UV illumination, are shown in Figure S4 (Supporting Information). Schottky barriers are expected to be formed at the metal (Au) and semiconductor (ZnO interface ($\Phi_{m(Au)}$ = ≈5.1 eV, $\chi_{s(ZnO)}$ ≈ 4.5 eV, leading to a potential barrier height of ≈0.6 eV). A symmetrical rectifying behavior is observed under dark condition with low current, and an almost linear shape (near-ohmic) *I–V* curves were obtained under UV illumination due to the reduction in energy barriers.

Next, MEAs with 3-row micropillar-based PDs were fabricated using the same bottom-up method and the micropillar center-to-center distance was kept at 15 μm (Movie S1, Supporting Information). **Figure 3** demonstrates the schematics and SEM images of printed contact electrodes and micropillars (Figure 3a), PDs after growing ZnO NWs (Figure 3b,c), as well as the electrical characterization results (Figure 3d–f; Figure S5, Supporting Information). In this configuration, the sensing area was increased by approximately three times, from 1.3 × 10^{-5} to 4.4 × 10^{-5} cm^2 (channel width increased from 13 to 44 μm with the same channel length: 100 μm). Electrical characterizations were conducted

© 2023 The Authors. Advanced Materials published by Wiley-VCH GmbH

15214095, 2023, 26, Downloaded from https://onlinelibrary.wiley.com/doi/10.1002/adma.202210711 by Test, Wiley Online Library on [07/07/2023]. See the Terms and Conditions (https://onlinelibrary.wiley.com/terms-and-conditions) on Wiley Online Library for rules of use; OA articles are governed by the applicable Creative Commons License

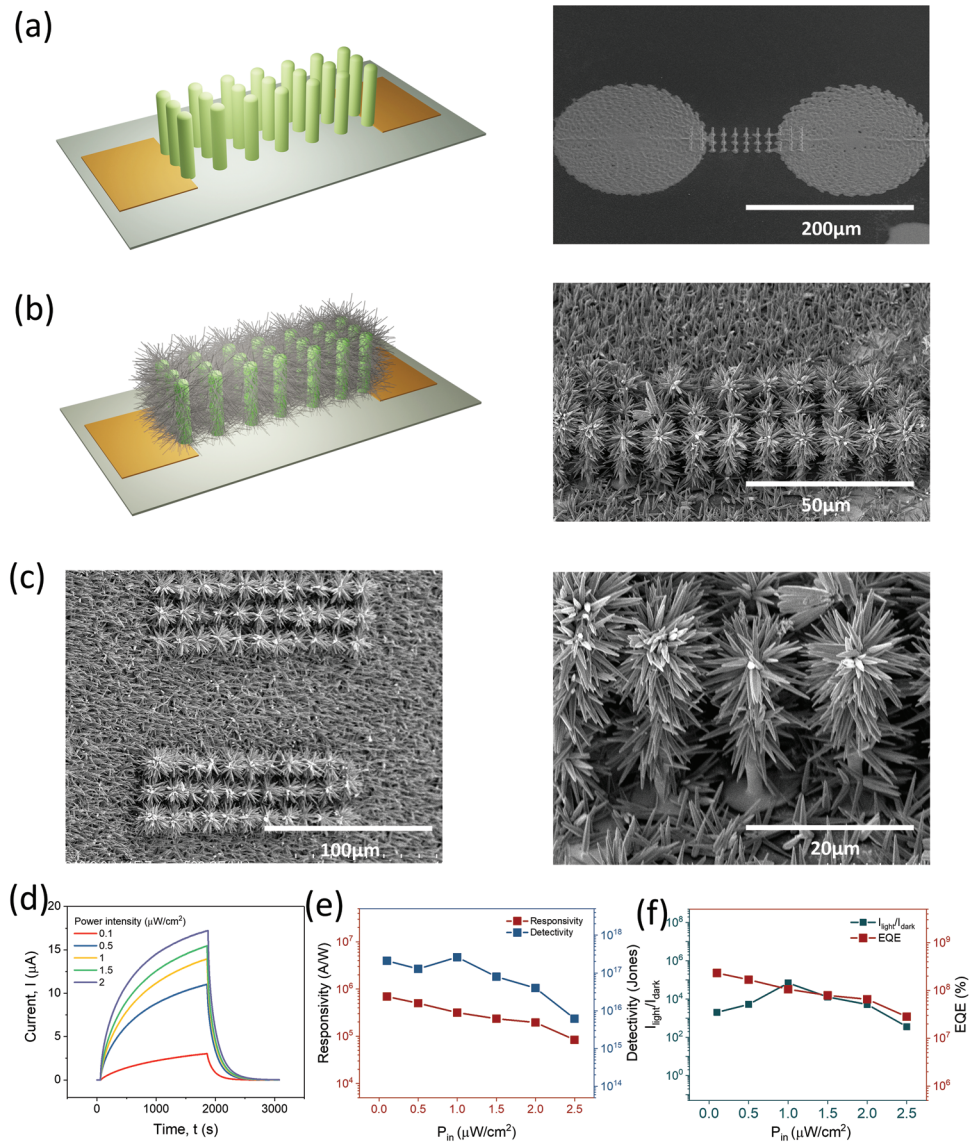

Figure 3. a) Schematic and SEM image of printed micropillars and contact electrodes. b) Schematic and SEM images of fabricated out-of-plane PDs after growing ZnO NWs on printed micropillars. c) SEM images of top and tilted side views of printed pillars and contact electrodes. d–f) Device characterization including time-domain photoresponse (d), and extracted values of responsivity and detectivity (e), and I_{light}/I_{dark} and EQE (f) under different light illumination from 0.1 to 2.5 μW cm^{-2}.

at 0.1 V bias. Interestingly, even with 10 times smaller applied bias voltage, the device detectivity showed an increment of two orders whereas I_{light}/I_{dark} ratio shows three orders of enhancement as compared to the results shown in Figure 2.

The out-of-plane ZnO NW-based PD performance was compared with the other state-of-the-art 3D UV PDs and 2D-printed PDs and the results are presented in **Figure 4** and summarized in **Table 2**. So far, the reported 3D PDs have been obtained by hydrothermally grown ZnO NWs on crystalline 3C-SiC or spin-coating ZnO quantum dots (QDs) on Au nanostructure/anodic aluminum oxide (AAO) matrix. They have been fabricated only on rigid substrates through multiple lithography and etching steps.[26,27] The 2D-printed PDs have been recently studied using inkjet, screen, and gravure printing.[28–42] Noticeably, most of the flexible 2D-printed PDs exhibit relatively lower responsivity and require a higher bias voltage. As the only flexible PD with 3D-printed or out-of-plane architectures, this work presents one of the best photoresponsive performance, exhibiting responsivity (3.16×10^5 A W^{-1}), detectivity (2.62×10^{17} Jones), and EQE (1.06×10^8%) using low bias voltage (0.1 V) under low light intensity (1 μW cm^{-2}). This is attributed to the high-aspect-ratio micropillars that provide the "base" for NWs and allows the creation of countless NW–NW junctions in a 3D space. The numerous energy barriers existence in the sensing channel for the free charge carrier results in the reduction of dark current and large change in device current under UV light illumination.

The photoresponse characteristics were also investigated under different temperatures (15, 30, 40, and 50 °C) (Figure S6,

© 2023 The Authors. Advanced Materials published by Wiley-VCH GmbH

15214095, 2023, 26, Downloaded from https://onlinelibrary.wiley.com/doi/10.1002/adma.202210711 by Test, Wiley Online Library on [07/07/2023]. See the Terms and Conditions (https://onlinelibrary.wiley.com/terms-and-conditions) on Wiley Online Library for rules of use; OA articles are governed by the applicable Creative Commons License

Table 2. The 3D-printed flexible PDs performance comparison with the state-of-the-art PDs fabricated in 3D and 2D configurations.

2D/3D	R (A W^{-1})	D^* [Jones]	I_{light}/I_{dark}	EQE [%]	Printed	Flexible	Materials	Intensity [μW cm^{-2}]	Bias Voltage [V]	Reference
3D	3.16×10^5	2.62×10^{17}	6.95×10^4	1.06×10^8	EHD	yes	Au/ZnO	1	0.1	This work
3D	0.66	N/A	N/A	225	NO	no	Au/ZnO	6900	10	[27]
3D	4.8×10^5	N/A	187.8	1.69×10^8	NO	no	SiC/ZnO	2.61	2	[26]
2D	$\approx 10^{-4}$	8.14×10^8	13.4	N/A	Screen Printing	yes	ZnO	3800	10	[28]
2D	7.5×10^6	3.3×10^{17}	10^6	N/A	Inkjet	yes	ZnO	9.1	1	[29]
2D	6.4	N/A	10^3	N/A	Inkjet	yes	ZnO/TPU	1000	5	[30]
2D	2.2	2.00×10^{11}	10^3	N/A	Inkjet	no	ZnO	2.2	5	[31]
2D	0.004	1.45×10^{10}	N/A	N/A	Inkjet	yes	ZnO/Ag	715	20	[32]
2D	0.14	N/A	10^{-3}	N/A	Inkjet	yes	ZnO	500	60	[33]
2D	2.7	N/A	3538	N/A	Inkjet	no	WO_3	0.27	5	[34]
2D	148	N/A	N/A	N/A	Screen Printing	no	ZnO	1000	10	[35]
2D	0.35	N/A	N/A	N/A	Inkjet	no	ZnO	1000	0.5	[36]
2D	383.6	N/A	2470	N/A	Inkjet	no	ZnO	520	5	[37]
2D	1.01	N/A	N/A	N/A	Gravure printing	yes	ZnO	127	10	[38]
2D	0.92	6.19×10^{11}	5.60×10^2	N/A	Gravure	yes	PBDTT-*ff*Qx/PCBM	N/A	10	[39]
2D	3386	N/A	N/A	1.20×10^4	Inkjet	no	ZnO	50	3	[40]
2D	1.62	7.77×10^{12}	1.83×10^4	N/A	Gravure	yes	Perovskite	N/A	10	[41]
2D	97.5	N/A	N/A	35 580	Inkjet	no	ZnO	N/A	4	[42]

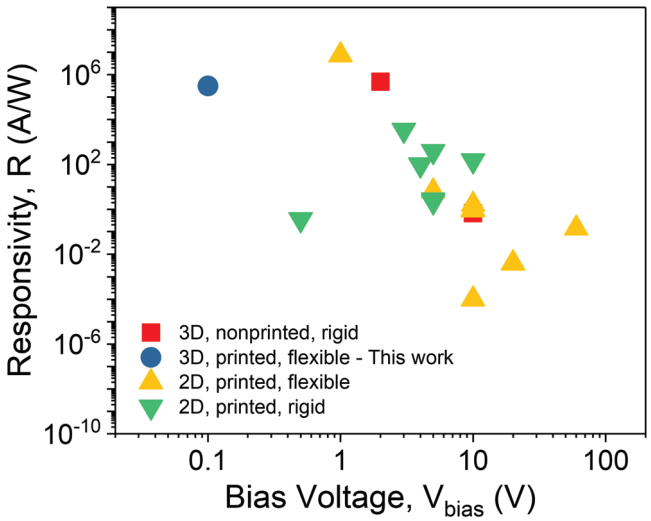

Figure 4. Responsivity comparison between this work and other 3D configuration and 2D-printed PDs reported in literature.

Supporting Information) at the light intensity of 0.1 μW cm^{-2}. Overall, the experimental results indicate a good thermally stable behavior of PDs under different temperatures although a slight increase of dark and light current is noticed. The increase in the dark current with an increase in temperature is expected because charge carriers acquire higher kinetic energy with higher temperatures. As a result, the electrons could easily overcome the potential barrier between NW–NW junctions and metal–NW interface and thus, the thermionic emission current increases. Nevertheless, a negligible perturbation was observed in the extracted R, D^*, EQE, and I_{Light}/I_{Dark} ratio.

The omnidirectional light-harvesting capability of the 3D PDs was shown by recording their angle-dependent optical response. The wide-angle photoresponse was recorded with the light source positioned at the normal position, ±30°, ±60°, and ±90° along the x- and y-axes. **Figure 5**a presents the schematic of the experimental setup and Figure S7 (Supporting Information) shows the photograph of the measurement setup. Figure 5b,c depicts the extracted normalized responsivity for all angles and fitted curves. The fitted curves demonstrate a symmetrical function for results obtained along both axes. Interestingly, in comparison with the response at the 0° light-source position (when the UV source is parallel with the device), the device responsivity tends to decrease as the incident angle increases for both axes. The observed variation in responsivity at different incident angles is caused by the change in the refractive index profile.[43] Most importantly, the PDs' responsivity remained high (≈20% of the responsivity at normal position), despite the variation, even in extreme cases of under ±90° light illumination, thus showing a strong capability of absorbing and detecting omnidirectional light sources over a broad incident angle due to the arrays of hierarchical structures, increased sensing areas as well as enhanced light–NW interaction.[44] Such excellent light absorption and omnidirectional detection capabilities present an advanced functionality compared with traditional 2D devices and can be advantageous for the development of 3D smart optoelectronic, efficient solar cells, artificial photosynthesis, and artificial intelligent systems. For example, the out-of-plane NW network on the flexible solar cells offers unique advantages in terms of strong light capture and harvest, even in extreme cases of ±90° light illumination, and thus could offer the opportunity to improve their conversion efficiency.[45] The 1D semiconductor NWs, with direct wire paths for charge transport and high surface area for light harvest, are emerging as a promising candidate for building photovoltaic (PV) cells. In fact, ZnO NWs have also been adopted in

© 2023 The Authors. Advanced Materials published by Wiley-VCH GmbH

15214095, 2023, 26, Downloaded from https://onlinelibrary.wiley.com/doi/10.1002/adma.202210711 by Test, Wiley Online Library on [07/07/2023]. See the Terms and Conditions (https://onlinelibrary.wiley.com/terms-and-conditions) on Wiley Online Library for rules of use; OA articles are governed by the applicable Creative Commons License

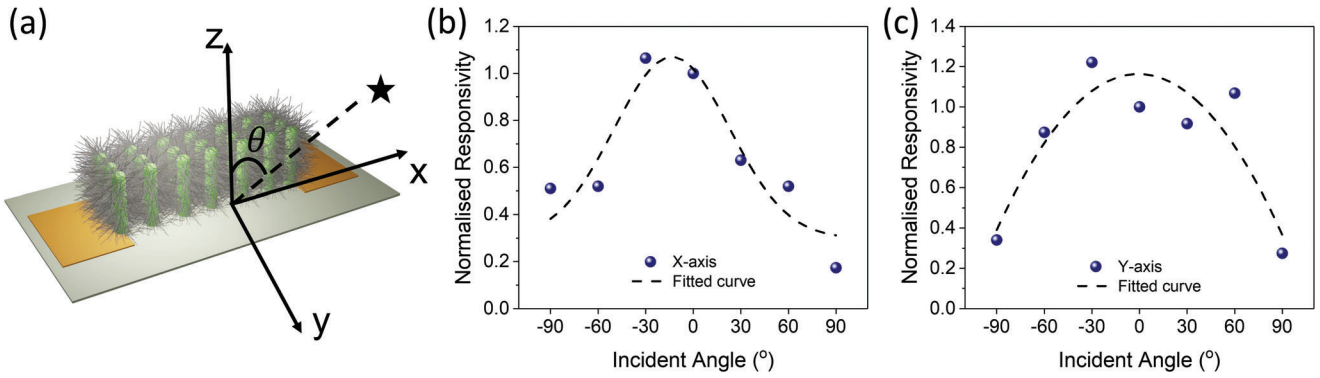

Figure 5. Wide-angle sensing measurements. a) Schematic of the wide-angle sensing measurement, showing the light source set at an angle along the *x*- and *y*-axes. b,c) Normalized responsivity extracted from angular response: b) along the *x*-axis; c) along the *y*-axis.

dye-sensitized solar cells (DSSCs) and the out-of-plane presence of such NWs, as shown here, will further advance the research in this area.[44] Next, similar electrical characterizations were conducted under bending conditions (40 mm radius curvature). With the sample mounted on 3D-printed concave and convex bending tools (**Figure 6**a), photoresponse is studied under different light intensities, from 0.1 to 2.0 μW cm^{-2}. Figure 6b shows the time-domain photoresponse curves set at 0.1 V_{bias} and 1 μW cm^{-2} light illumination under concave and convex conditions. It is apparent that devices under tconvex condition present a slightly lower photocurrent but faster response/recovery time. The minor decrease in photocurrent is owing to the slight increase in the sensing area (channel width reduced from 44 to 48 μm with the fixed 100 μm channel length). Moreover, the response/recovery time has dramatically decreased owing to more spaced-out NWs and potentially smoother carrier transport pathways. Further, devices were tested under bending (concave and convex) conditions with strains applied perpendicular to the sensing channel (Figure S8, Supporting Information). The response/recovery time shows a similar trend as in the case of the strain parallel to the sensing channel. However, the change in the photocurrent is negligible when compared to the devices under the parallel strain. This is probably because the sensing area remains approximately unchanged for planar, concave and convex conditions when the strain is applied perpendicular to the channel. This leads to a negligible change of the device performance under both concave and convex conditions. Nevertheless, all parameters extracted (*R*, *D**, EQE, and I_{light}/I_{dark}) under different bending and strain conditions reveal a stable performance and insignificant difference.

3. Conclusion

We have established a robust 3D printing methodology for constructing high-aspect-ratio Au-based micropillar electrode arrays (MEAs) on flexible substrates and used them to grow out-of-the-plane NW networks by employing the seedless hydrothermal synthesis. The developed method could be used to obtain different shapes of multi-length-scale out-of-plane architectures with different spacings. The presented printing approach is versatile and can be used for applications such as high-resolution interconnects for heterogenous integration or the out-of-plane NW network coating to trap or soak the light. The 3D hierarchical functional architecture is expected to enhance the light scattering events and thus, leading to a higher trapping of the incident omnidirectional light (to enhance the light flux). Therefore, the method can be employed to enhance the energy harvesting efficiency of solar cells and artificial photosynthesis processes. To demonstrate this, the fabricated hierarchical architectures were employed to fabricate 3D flexible UV photodetectors (PDs). The fabricated 3D PDs' sensing performance was tested over wide light incident angles (±90°). The photocurrent ratios at an incident angle to normal incidence were extracted and have exhibited good omnidirectional light-absorption ability. Furthermore, the 3D PDs were tested under both concave and convex bending conditions and demonstrated excellent mechanical flexibility with negligible changes in performance. The presented study demonstrates the potential of high resolution EHD-based jet printing toward 3D conductive and functional structure fabrication and opens new directions for high-performance flexible electronics.

4. Experimental Section

Electrohydrodynamic (EHD)-Based Jet Printing: In this work, a super inkjet (SIJ) printing system was used to print libraries of out-of-plane micropillar electrode arrays (MEAs). The pillar printing was conducted using super fine nozzles (1–3 μm-diameter opening size) with gold nanoparticle (Au NP) ink (CAu-2000, ULVAC Technologies) under ambient conditions (room temperature, humidity: ≈40%). The optimized printing parameters for constructing high-aspect-ratio pillars are: 75% square waveform, 320 V amplitude, 0 DC bias, 20 Hz frequency, 1 mm s^{-1} work stage speed, and 10 mm s^{-2} acceleration. After the micropillars were printed, the substrate was annealed at 250 °C for 2 h to cure the ink.

ZnO NW Synthesis: The hydrothermal approach was adopted for the synthesis of ZnO NWs on printed Au MEAs using a growth solution containing 1:1 ratio of 100 mM zinc nitrate hexahydrate ($Zn(NO_3)_2$, $6H_2O$, 98%, Sigma–Aldrich), and 100 mM hexamethylenetetramine (HMTA, Sigma–Aldrich). 1 mL of a 40 mM ammonium hydroxide (NH_4OH, Sigma–Aldrich) solution was also added to the growth solution. During the NW growth, the substrates were immersed facing down in a Teflon flask with growth solution, sealed inside stainless-steel autoclave reactor, and placed in a preheated convection oven at 95 °C and left inside for 15 h. The autoclave was then taken out from the oven and allowed to cool down naturally.

Morphological Characterization: The morphological analysis of pillar optimization, ZnO NWs, and fabricated PDs was performed using scanning electron microscopy (SEM-Hitachi SU8240).

© 2023 The Authors. Advanced Materials published by Wiley-VCH GmbH

15214095, 2023, 26, Downloaded from https://onlinelibrary.wiley.com/doi/10.1002/adma.202210711 by Test, Wiley Online Library on [07/07/2023]. See the Terms and Conditions (https://onlinelibrary.wiley.com/terms-and-conditions) on Wiley Online Library for rules of use; OA articles are governed by the applicable Creative Commons License

15214095, 2023, 26, Downloaded from https://onlinelibrary.wiley.com/doi/10.1002/adma.202210711 by Test, Wiley Online Library on [07/07/2023]. See the Terms and Conditions (https://onlinelibrary.wiley.com/terms-and-conditions) on Wiley Online Library for rules of use; OA articles are governed by the applicable Creative Commons License

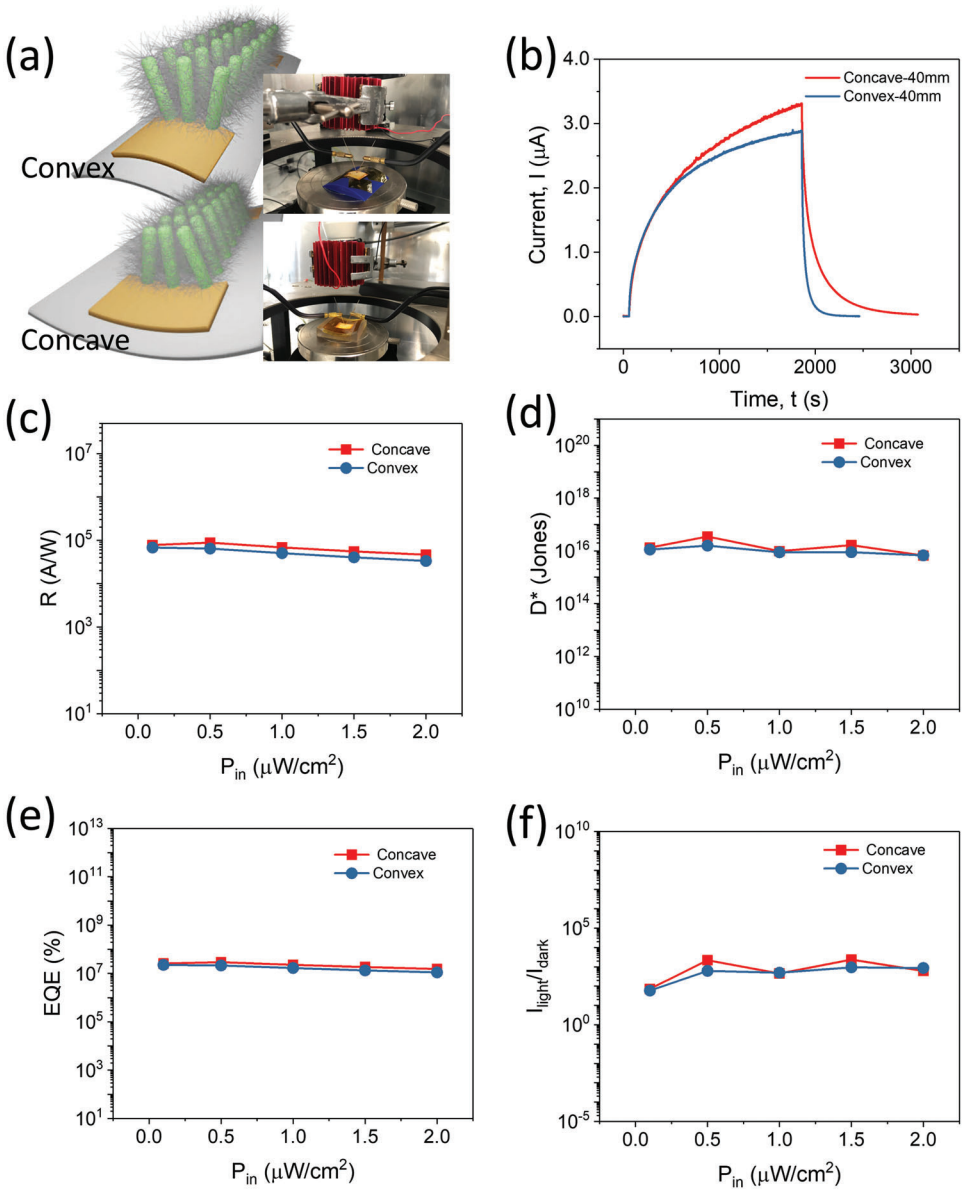

Figure 6. Photoresponse under 40 mm concave and convex bending conditions. a) Schematic and the experimental arrangement during electrical measurements. b) Time-domain photoresponse curves recorded at $0.1V_{bias}$ and 1 μW cm^{-2} light illumination. c–f) Extracted parameters for both bending conditions including: c) *R*; d) *D**; e) EQE; and f) I_{light}/I_{dark}.

PD Fabrication: First, the device substrates were prepared by spin-coating polyimide (PI-2545, HD microsystems) on glass substrates at 2000 rpm for 60 s. After soft baking at 120 °C for 2 min, a second layer was spin coated under similar coating conditions. Spin-on PI was subsequently cured in the oven at 300 °C with a slow ramp rate of 4 °C min^{-1}. Next, PD contact electrodes and MEAs were printed using EHD printing system and Au ink. After, the NWs were synthesized on cured MEAs to realize out-of-plane architectures. Finally, the spin-on PI was released from the glass substrates by dipping in DI water for 2 min to develop 3D flexible PDs.

Electrical Characterization: The electrical characterization of PDs was conducted using a UV light-emitting diode (wavelength: 365 nm) under ambient conditions. Photoresponse measurements were completed using a Cascade Micro-tech Auto-guard probe station interfaced with a semiconductor device parameter analyzer (B1500A, Agilent). Photoresponse characteristics under different temperatures were conducted by placing the device on the Linkam PE120 Peltier system.

Supporting Information

Supporting Information is available from the Wiley Online Library or from the author.

Acknowledgements

This work was supported in part by Engineering and Physical Sciences Research Council (EPSRC) through Engineering Fellowship for Growth

 © 2023 The Authors. Advanced Materials published by Wiley-VCH GmbH

(EP/R029644/1) and Hetero-print Programme Grant (EP/R03480X/1). This work was started by R.D's Bendable Electronics and Sensing Technologies (BEST) Group when he was at University of Glasgow. The work was completed after he moved to Northeastern University, where his group is known as the Bendable Electronics and Sustainable Technologies (BEST) Group.

Conflict of Interest

The authors declare no conflict of interest.

Data Availability Statement

The data that support the findings of this study are available from the corresponding author upon reasonable request.

Keywords

flexible electronics, omnidirectional light sensing, out-of-plane electronics, photodetectors, printed micropillars

Received: November 17, 2022
Revised: February 6, 2023
Published online: May 13, 2023

[1] a) T. Someya, Z. Bao, G. G. Malliaras, *Nature* **2016**, *540*, 379; b) S.-T. Han, H. Peng, Q. Sun, S. Venkatesh, K.-S. Chung, S. C. Lau, Y. Zhou, V. A. L. Roy, *Adv. Mater.* **2017**, *29*, 1700375; c) A. Paul, N. Yogeswaran, R. Dahiya, *Adv. Intell. Syst.* **2022**, *4*, 2200183; d) J. Neto, R. Chirila, A. S. Dahiya, A. Christou, D. Shakthivel, R. Dahiya, *Adv. Sci.* **2022**, *9*, 2201525; e) M. Chakraborty, F. Nikbakhtnasrabadi, R. Dahiya, *IEEE J. Flexible Electron.* **2022**, *1*, 107.

[2] a) F. Liu, S. Deswal, A. Christou, Y. Sandamirskaya, M. Kaboli, R. Dahiya, *Sci. Rob.* **2022**, *7*, eabl7344; b) S. Ma, Y. Kumaresan, A. S. Dahiya, R. Dahiya, *Adv. Electron. Mater.* **2022**, *8*, 2101029.

[3] a) S. Jesse, A. Y. Borisevich, J. D. Fowlkes, A. R. Lupini, P. D. Rack, R. R. Unocic, B. G. Sumpter, S. V. Kalinin, A. Belianinov, O. S. Ovchinnikova, *ACS Nano* **2016**, *10*, 5600; b) Y. Lu, S. C. Chen, *Adv. Drug Delivery Rev.* **2004**, *56*, 1621; c) J. Shi, A. R. Votruba, O. C. Farokhzad, R. Langer, *Nano Lett.* **2010**, *10*, 3223; d) L. Hui, Q. Zhang, W. Deng, H. Liu, *Small* **2019**, *15*, 1805428; e) E. C. Nelson, N. L. Dias, K. P. Bassett, S. N. Dunham, V. Verma, M. Miyake, P. Wiltzius, J. A. Rogers, J. J. Coleman, X. Li, P. V. Braun, *Nat. Mater.* **2011**, *10*, 676; f) Q. Pan, M. Su, Z. Zhang, B. Chen, Z. Huang, X. Hu, Z. Cai, Y. Song, *Adv. Mater.* **2020**, *32*, 1907280; g) C. Becker, D. Karnaushenko, T. Kang, D. D. Karnaushenko, M. Faghih, A. Mirhajivarzaneh, O. G. Schmidt, *Sci. Adv.* **2019**, *5*, eaay7459; h) C. Becker, B. Bao, D. D. Karnaushenko, V. K. Bandari, B. Rivkin, Z. Li, M. Faghih, D. Karnaushenko, O. G. Schmidt, *Nat. Commun.* **2022**, *13*, 2121; i) W. Lee, Y. Liu, Y. Lee, B. K. Sharma, S. M. Shinde, S. D. Kim, K. Nan, Z. Yan, M. Han, Y. Huang, Y. Zhang, J.-H. Ahn, J. A. Rogers, *Nat. Commun.* **2018**, *9*, 1417; j) M. A. Skylar-Scott, S. Gunasekaran, J. A. Lewis, *Proc. Natl. Acad. Sci. USA* **2016**, *113*, 6137.

[4] M. Kim, G. J. Lee, C. Choi, M. S. Kim, M. Lee, S. Liu, K. W. Cho, H. M. Kim, H. Cho, M. K. Choi, N. Lu, Y. M. Song, D.-H. Kim, *Nat. Electron.* **2020**, *3*, 546.

[5] a) Y. K. Mishra, R. Adelung, *Mater. Today* **2018**, *21*, 631; b) K. Sun, Y. Jing, C. Li, X. Zhang, R. Aguinaldo, A. Kargar, K. Madsen, K. Banu, Y. Zhou, Y. Bando, Z. Liu, D. Wang, *Nanoscale* **2012**, *4*, 1515.

[6] B. W. An, K. Kim, H. Lee, S.-Y. Kim, Y. Shim, D.-Y. Lee, J. Y. Song, J.-U. Park, *Adv. Mater.* **2015**, *27*, 4322.

[7] C. Zhang, S. Liu, G. Li, C. Zhang, X. Liu, J. Luo, *Adv. Mater.* **2018**, *30*, 1801328.

[8] a) H. Mao, D. Wu, W. Wu, J. Xu, Y. Hao, *Nanotechnology* **2009**, *20*, 445304; b) Y. Hong, D. Zhao, D. Liu, B. Ma, G. Yao, Q. Li, A. Han, M. Qiu, *Nano Lett.* **2018**, *18*, 5036; c) Y. Ofir, I. W. Moran, C. Subramani, K. R. Carter, V. M. Rotello, *Adv. Mater.* **2010**, *22*, 3608.

[9] a) E. Mullen, M. A. Morris, *Nanomaterials* **2021**, *11*, 1085; b) M. Chakraborty, J. Kettle, R. Dahiya, *IEEE J. Flexible Electron.* **2022**, *1*, 4; c) F. Liu, S. Deswal, A. Christou, R. Chirila, M. S. Baghini, D. Shakthivel, M. Chakraborty, R. Dahiya, *Sci. Rob.* **2022**, *7*, eabl7286.

[10] D. Shakthivel, A. S. Dahiya, R. Mukherjee, R. Dahiya, *Curr. Opin. Chem. Eng.* **2021**, *34*, 100753.

[11] A. S. Dahiya, D. Shakthivel, Y. Kumaresan, A. Zumeit, A. Christou, R. Dahiya, *Nano Converg.* **2020**, *7*, 33.

[12] X. Chen, J. M. Lawrence, L. T. Wey, L. Schertel, Q. Jing, S. Vignolini, C. J. Howe, S. Kar-Narayan, J. Z. Zhang, *Nat. Mater.* **2022**, *21*, 811.

[13] L. Grob, H. Yamamoto, S. Zips, P. Rinklin, A. Hirano-Iwata, B. Wolfrum, *Adv. Mater. Technol.* **2020**, *5*, 1900517.

[14] a) C. Wei, J. Dong, *J. Manuf. Process* **2014**, *16*, 257; b) M. S. Onses, E. Sutanto, P. M. Ferreira, A. G. Alleyne, J. A. Rogers, *Small* **2015**, *11*, 4237; c) B. Zhang, J. He, X. Li, F. Xu, D. Li, *Nanoscale* **2016**, *8*, 15376.

[15] B. Zhang, B. Seong, J. Lee, V. Nguyen, D. Cho, D. Byun, *ACS Appl. Mater. Interfaces* **2017**, *9*, 29965.

[16] a) A. S. Dahiya, S. Boubenia, G. Franzo, G. Poulin-Vittrant, S. Mirabella, D. Alquier, *Nanoscale Res. Lett.* **2018**, *13*, 249; b) A. Kargar, Y. Jing, S. J. Kim, C. T. Riley, X. Pan, D. Wang, *ACS Nano* **2013**, *7*, 11112; c) Y. Peng, J. Lu, X. Wang, W. Ma, M. Que, Q. Chen, F. Li, X. Liu, W. Gao, C. Pan, *Nano Energy* **2022**, *94*, 106945; d) D. Shakthivel, W. T. Navaraj, S. Champet, D. H. Gregory, R. Dahiya, *Nanoscale Adv.* **2019**, *1*, 3568.

[17] a) L. Tian, Q. Xin, C. Zhao, G. Xie, M. Z. Akram, W. Wang, R. Ma, X. Jia, B. Guo, J. R. Gong, *Small* **2021**, *17*, 2006530; b) H. Zhou, C. Xiao, Z. Yang, Y. Du, *Nanotechnology* **2020**, *31*, 282001.

[18] Y. Han, C. Wei, J. Dong, *Manuf. Lett.* **2014**, *2*, 96.

[19] P. Ren, J. Dong, *Adv. Mater. Technol.* **2021**, *6*, 2100280.

[20] D. Wang, Q. Wang, Q. Meng, K. Li, J. Li, S. Xiong, C. Liu, X. Yuan, T. Ren, J. Liang, *J. Micromech. Microeng.* **2019**, *29*, 045012.

[21] A. Reiser, M. Lindén, P. Rohner, A. Marchand, H. Galinski, A. S. Sologubenko, J. M. Wheeler, R. Zenobi, D. Poulikakos, R. Spolenak, *Nat. Commun.* **2019**, *10*, 1853.

[22] P. Galliker, J. schneider, H. Eghlidi, S. Kress, V. sandoghdar, D. Poulikakos, *Nat. Commun.* **2012**, *3*, 890.

[23] C. Wei, H. Qin, C.-P. Chiu, Y.-S. Lee, J. Dong, *J. Manuf. Syst.* **2015**, *37*, 505.

[24] a) K. Murata, in *Polytronic 2007 - 6th Int. Conf. on Polymers and Adhesives in Microelectronics and Photonics*, IEEE, Piscataway, NJ, USA **2007**, pp. 293–296; b) K. Murata, K. Masuda, *Convertech e-Print* **2011**, *1*, 108.

[25] T. M. H. Nguyen, S. Kim, C. W. Bark, *J. Mater. Chem. A* **2021**, *9*, 1269.

[26] X. Zhang, B. Liu, W. Yang, W. Jia, J. Li, C. Jiang, X. Jiang, *Nanoscale* **2016**, *8*, 17573.

[27] M.-Y. Li, M. Yu, S. Jiang, S. Liu, H. Liu, H. Xu, D. Su, G. Zhang, Y. Chen, J. Wu, *Mater. Horiz.* **2020**, *7*, 905.

[28] C.-H. Lin, D.-S. Tsai, T.-C. Wei, D.-H. Lien, J.-J. Ke, C.-H. Su, J.-Y. Sun, Y.-C. Liao, J.-H. He, *ACS Nano* **2017**, *11*, 10230.

[29] X. Liu, L. Gu, Q. Zhang, J. Wu, Y. Long, Z. Fan, *Nat. Commun.* **2014**, *5*, 4007.

[30] D.-H. Lien, H.-P. Wang, S.-B. Chen, Y.-C. Chi, C.-L. Wu, G.-R. Lin, Y.-C. Liao, J.-H. He, *npj Flexible Electron.* **2018**, *2*, 19.

[31] B. Cook, M. Gong, A. Corbin, D. Ewing, A. Tramble, J. Wu, *ACS Omega* **2019**, *4*, 22497.

© 2023 The Authors. Advanced Materials published by Wiley-VCH GmbH

15214095, 2023, 26, Downloaded from https://onlinelibrary.wiley.com/doi/10.1002/adma.202210711 by Test, Wiley Online Library on [07/07/2023]. See the Terms and Conditions (https://onlinelibrary.wiley.com/terms-and-conditions) on Wiley Online Library for rules of use; OA articles are governed by the applicable Creative Commons License

[32] H.-C. Wang, Y. Hong, Z. Chen, C. Lao, Y. Lu, Z. Yang, Y. Zhu, X. Liu, *Nanoscale Res. Lett.* **2020**, *15*, 176.
[33] Y. Dong, Y. Zou, J. Song, J. Li, B. Han, Q. Shan, L. Xu, J. Xue, H. Zeng, *Nanoscale* **2017**, *9*, 8580.
[34] B. Cook, Q. Liu, J. Butler, K. Smith, K. Shi, D. Ewing, M. Casper, A. Stramel, A. Elliot, J. Wu, *ACS Appl. Mater. Interfaces* **2018**, *10*, 873.
[35] Q. Guo, Y. Zhao, G. Wang, D. Chen, H. Zhao, C. Jiang, G. Huang, Z. Di, Y. Mei, *Appl. Phys. Lett.* **2019**, *115*, 122106.
[36] J. Nahlik, A. Laposa, J. Voves, J. Kroutil, J. Drahokoupil, M. Davydova, *IEEE Sens. J.* **2019**, *19*, 5587.
[37] B. Cook, Q. Liu, M. Gong, D. Ewing, M. Casper, A. Stramel, J. Wu, *ACS Appl. Mater. Interfaces* **2017**, *9*, 23189.
[38] J. Park, J. Lee, Y. Noh, K.-H. Shin, D. Lee, *J. Mater. Chem. C* **2016**, *4*, 7948.
[39] S. Tong, J. Yuan, C. Zhang, C. Wang, B. Liu, J. Shen, H. Xia, Y. Zou, H. Xie, J. Sun, S. Xiao, J. He, Y. Gao, J. Yang, *npj Flexible Electron.* **2018**, *2*, 7.
[40] M. R. Alenezi, A. S. Alshammari, T. H. Alzanki, P. Jarowski, S. J. Henley, S. R. P. Silva, *Langmuir* **2014**, *30*, 3913.
[41] S. Tong, C. Gong, C. Zhang, G. Liu, D. Zhang, C. Zhou, J. Sun, S. Xiao, J. He, Y. Gao, J. Yang, *Appl. Mater. Today* **2019**, *15*, 389.
[42] B. Cook, M. Gong, D. Ewing, M. Casper, A. Stramel, A. Elliot, J. Wu, *ACS Appl. Nano Mater.* **2019**, *2*, 3246.
[43] S. Lim, D.-S. Um, M. Ha, Q. Zhang, Y. Lee, Y. Lin, Z. Fan, H. Ko, *Nano Res.* **2017**, *10*, 22.
[44] S. H. Ko, D. Lee, H. W. Kang, K. H. Nam, J. Y. Yeo, S. J. Hong, C. P. Grigoropoulos, H. J. Sung, *Nano Lett.* **2011**, *11*, 666.
[45] K.-Q. Peng, S.-T. Lee, *Adv. Mater.* **2011**, *23*, 198.

© 2023 The Authors. Advanced Materials published by Wiley-VCH GmbH

15214095, 2023, 26, Downloaded from https://onlinelibrary.wiley.com/doi/10.1002/adma.202210711 by Test, Wiley Online Library on [07/07/2023]. See the Terms and Conditions (https://onlinelibrary.wiley.com/terms-and-conditions) on Wiley Online Library for rules of use; OA articles are governed by the applicable Creative Commons License